# **Testing Earthquake Nucleation Length Scale with Pawnee Aftershocks**

Bill S. Wu<sup>1</sup> and Gregory C. McLaskey<sup>\*1</sup>

#### **Abstract**

The interpretation of precursory seismicity can depend on a critical nucleation length scale  $h^*$ , yet  $h^*$  is largely unconstrained in the seismogenic crust. To estimate  $h^*$  and associated earthquake nucleation processes at 2-7 km depths in Oklahoma, we studied seismic activity occurring prior to nine M 2.5-3.0 earthquakes that are aftershocks of the 3 September 2016 M 5.8 Pawnee, Oklahoma, earthquake. Four of the nine M 2.5-3.0 aftershocks studied did not have detectable seismicity within a 2 km radius of their hypocenters in the preceding 16 hr time windows. For the other five events, which did exhibit foreshock sequences, we estimated the static stress changes associated with each event of each sequence based on precise earthquake relocations and magnitude estimates. By carefully examining the spatiotemporal characteristics, we found all five of these M 2.5-3.0 aftershocks, and 70% of our studied events were plausibly triggered via static stress transfer from nearby earthquakes occurring hours to seconds earlier, consistent with the cascade nucleation model and a small  $h^*$  in this region. The smallest earthquakes we could quantitatively study were M -1.5 events, which likely have 1-2 m rupture dimensions. The existence of these small events also supports a small nucleation length scale  $h^* \le 1$  m, consistent with laboratory estimates. However, our observations cannot rule out more complicated earthquake initiation processes involving interactions between foreshocks and slow slip. Questions also remain as to whether aftershocks initiate differently from more isolated earthquakes.

Cite this article as Wu, B. S., and G. C. McLaskey (2022). Testing Earthquake Nucleation Length Scale with Pawnee Aftershocks, *Seismol. Res. Lett.* 93, 2147–2160, doi: 10.1785/0220210184.

**Supplemental Material** 

#### Introduction

The way that earthquakes start and the role that foreshocks might play in that process is thought to depend on a critical nucleation length scale  $h^*$  that is a function of friction parameters, stress conditions, and elastic properties of the fault rocks, as described in equation (1). A small  $h^*$  (meter scale) suggests a cascade foreshock model, in which small foreshocks and larger earthquakes initiate in an identical fashion (Ellsworth and Beroza, 1995; Beroza and Ellsworth, 1996). This model suggests that foreshocks are earthquakes that trigger each other (and the mainshock) through static stress transfer without a widespread aseismic slip component. A large  $h^*$  (kilometer scale) is more consistent with the preslip model (Ellsworth and Beroza, 1995; Beroza and Ellsworth, 1996). In the preslip model, foreshocks are triggered by aseismic slip, typically attributed to the extended nucleation of a large earthquake; so this model can explain prolonged foreshock sequences and their migration, sometimes observed prior to large subduction zone earthquakes (e.g., Kato et al., 2012; Ruiz et al., 2014; Schurr et al., 2014). However, the coexistence of a large earthquake that hypothetically requires a kilometer-sized nucleation region and smaller foreshocks that also rupture dynamically requires heterogeneous fault properties that likely complicate

the physics beyond what the laboratory and theoretical studies display (McLaskey, 2019).

Here, we consider the spatiotemporal patterns of seismicity and the previous foreshock models primarily as a way to help constrain  $h^*$  in the seismogenic crust and to test if the seismic observations are consistent with estimates of  $h^*$  based on laboratory-derived parameters. Although the techniques outlined in this work might be applicable to other faulting environments, we focus this study on north-central Oklahoma, United States, where fluid injection has contributed to a number of large earthquakes in recent years.

## **Background on Nucleation Length Scale**

Theoretical considerations indicate that earthquakes begin slowly, with stable fault slip that precedes dynamic fault rupture (Ida, 1972; Andrews, 1978; Dieterich 1992; Rubin and Ampuero, 2005). This slow nucleation phase has been observed in laboratory earthquake experiments (Okubo and Dieterich, 1984;

<sup>1.</sup> School of Civil and Environmental Engineering, Cornell University, Ithaca, New York, U.S.A.

<sup>\*</sup>Corresponding author: gcm8@cornell.edu

<sup>©</sup> Seismological Society of America

Ohnaka and Kuwahara, 1990; Nielsen *et al.*, 2010; McLaskey, 2019). These works show an early phase characterized by slow slip and low-rupture velocities until the ruptured region expands to the critical length  $h^*$  (also termed  $L_c$ ), and a later phase during which rupture velocity rapidly increases to close to the speed of sound (Ohnaka and Kuwahara, 1990; Latour *et al.*, 2013; McLaskey and Kilgore, 2013). Theoretical arguments suggest that  $h^*$  has the form

$$h^* \sim \frac{GD_c}{\sigma_n f},\tag{1}$$

in which G is the shear modulus,  $\sigma_n$  is the effective normal stress, and  $D_c$  and f are frictional parameters. Although the precise definition f is somewhat debated, a common formulation is f = b - a (Rice, 1993; Scholz, 1998), in which b - a is the velocity dependence of steady state friction.

Laboratory experiments show that  $h^*$  is on the order of a meter for smooth, bare granite surfaces deformed at  $\sigma_n \sim$ 5 MPa (McLaskey, 2019). Granite is thought to be a representative rock for the continental crust and crystalline basement in Oklahoma, and if we scale  $\sigma_n$  to pressures expected at seismogenic depths (~100 MPa) and include friction parameters determined for wet granite at seismogenic pressures and temperatures (Blanpied et al., 1995), we expect  $h^* \sim 0.1$ –1 m. However, there is considerable uncertainty regarding the scaling of  $D_c$ ; it is thought to scale with fault roughness (e.g., Scholz, 1988) or thickness of the shear zone (Marone and Kilgore, 1993). Seismological studies have showed that a parameter related to fracture energy scales with earthquake size (Abercrombie and Rice, 2005), which could suggest  $D_c \sim 1 \text{ mm}$  ( $h^* \sim 100 \text{ m}$ ) for  $\mathbf{M} \sim 1-2$  earthquakes and  $D_c \sim 1 \text{ m}$  ( $h^* \sim 100 \text{ km}$ ) for M  $\sim 6$  earthquakes (Tinti et al., 2005, and references therein). However, those parameters likely reflect the combined effects of rupture initiation, propagation, and arrest (Ke et al., 2021), and may not be appropriate for characterizing earthquake initiation, which is arguably a more localized process that is independent of rupture arrest. Modeling studies have assumed  $h^*$  ranging from 2 to 20 m (Lui and Lapusta, 2016; Veedu and Barbot, 2016), up to 1 km (Tse and Rice, 1986; Barbot et al., 2012); however, this choice is strongly dictated by numerical tractability. Considering the above arguments,  $h^*$  at seismogenic depths is highly uncertain.

Bounding the seismogenic zone at very shallow depths, low  $\sigma_n$  and unconsolidated granular material likely produce much larger  $h^*$ . At great depths, above about 300°C,  $h^*$  becomes large or undefined when quartz begins to exhibit crystal plasticity and f becomes negative, that is, velocity strengthening (Scholz, 1998).

One in situ constraint on  $h^*$  is the existence of small earthquakes. Recent work (Wu and McLaskey, 2019) showed that for a small earth-quake to become fully dynamic (and not slow with low stress drop), the rupture radius a must be about  $5 \times$ larger than the nucleation length  $h^*$ . Earth-quakes with  $a \approx h^*$  remain slow, with low  $\Delta \sigma$ , and only weakly radiate seismic waves. Thus, the observation of small-magnitude standard seismic events with rupture radius a may place an upper bound on  $h^*$  (i.e.,  $h^* < a$ ).

However, fault heterogeneity may complicate the relationship between  $h^*$ , foreshocks, and a minimum earthquake dimension. Small seismic events might be the result of locally brittle fault conditions that cause a localized reduction in  $h^*$ , whereas the initiation of a larger earthquake might hypothetically be controlled by a larger, fault-average  $h^*$  and exhibit a larger nucleation region. This behavior was observed in laboratory experiments (McLaskey and Kilgore, 2013), and, if relevant to natural faults, it suggests that the spatial extent of the foreshock region may provide an estimate of the larger nucleation region (e.g., Dodge et al., 1996; Kato et al., 2012; Chen and Shearer, 2013; McLaskey and Lockner, 2018). Recent modeling studies have investigated the interplay between a larger aseismic nucleation process and smaller seismic events (Noda et al., 2013; Schaal and Lapusta, 2019; Cattania and Segall, 2021). Some studies show that the "kick" provided by small seismic events can facilitate an abrupt nucleation and circumvent a larger, slower nucleation process (Noda et al., 2013; McLaskey, 2019) and directly grow from small events (with small  $h^*$ ) into larger events (McLaskey and Lockner, 2014; Cattania and Segall, 2021). Therefore, even if the existence of small events does not place definitive bounds on fault-average  $h^*$ , it may offer a mechanism by which earthquakes can initiate with effectively small  $h^*$  and no large preslip region.

If  $h^*$  is indeed small ( $\sim$ 1 m) on continental faults, this suggests that foreshocks and nucleation will likely follow the cascade model (e.g., Landers 1992, Hector Mine 1999, Pawnee 2016, Ridgecrest 2019). We would expect any foreshocks to be tightly clustered in space and time similar to standard mainshock-aftershock sequences. Alternatively, if we observed extended swarms of foreshocks that are spatially isolated compared to their magnitudes, thus making stress transfer an unlikely triggering mechanism, we might suspect that widespread aseismic slip or some other factor was responsible for triggering those events. Some fault zones, particularly creeping fault segments and some subduction zones, are known to have more clay-rich minerology (Carpenter et al., 2011, Kameda et al., 2015), which can produce values of f that are near zero. Such conditions would promote large  $h^*$ , perhaps on the order of kilometers or tens of kilometers. Earthquake swarms and foreshocks on such faults may be better characterized by some form of the preslip model (e.g., Tohoku 2011, Iquique 2014, Valparaíso 2017).

## **Caveats to This Study**

In this work, we study seismic activity occurring before nine M 2.5–3.0 earthquakes that are aftershocks to the 3 September 2016 M 5.8 Pawnee, Oklahoma, earthquake. Each of these nine study events share common instrumentation and geologic

setting, so we collectively study the group of earthquakes and the variations between them, to sample the variability of initiation processes that might occur under nominally identical circumstances, and to better inform our estimates of  $h^*$  in the region. We built nine catalogs that focus on seismicity leading up to each of the nine study events, and study the spatial and temporal distribution of prior seismicity. Our approach follows previous work (e.g., Dodge *et al.*, 1996; Ellsworth and Bulut, 2018; Yoon *et al.*, 2019). However, we study events that are clearly aftershocks of the Pawnee earthquake, and this can affect the interpretation of our results.

First, some of the events we studied were likely directly triggered by the Pawnee earthquake due to Coulomb stress changes, dynamic shaking, or other processes. However, we focus our study on earthquakes occurring 12-31 days after the Pawnee mainshock when the earthquake rates associated with Coulomb stress changes are expected to be slowly declining (i.e., Dieterich, 1994). We must acknowledge that occasional events during this 12-31 day time period were likely directly triggered by the Pawnee mainshock, but rate increases associated with spatiotemporally localized earthquake clusters require a different driving mechanism. Most of the events in a cluster must either be aftershocks of aftershocks (in cases where events were plausibly triggered via static stress transfer within the cluster), or they must be triggered by something else, such as spatiotemporally localized slow slip. Distinguishing between those scenarios is the central aim of our analysis.

Second, our analysis assumes that event-to-event interactions within an aftershock sequence are controlled by the same physical mechanisms as those at play for more isolated earthquakes, just at an accelerated rate. Our results would thus be biased if aftershocks initiate in a different way from more isolated earthquakes. There is evidence showing that higher loading rate can effectively shrink  $h^*$  and cause earthquakes to initiate more abruptly (e.g., Kaneko and Lapusta, 2008; Guérin-Marthe *et al.*, 2019); however, a full comparison between inferences based on aftershocks and those made from more isolated sequences is outside the scope of this article. The Pawnee earthquake was also the result of wastewater injection; we assume here that the mechanics of the aftershocks we study are unaffected by the fluid injection in the region.

Finally, we do not claim that our observations or our estimates of  $h^*$  can be generalized to other faulting environments. Pawnee is an intraplate earthquake. We expect a larger  $h^*$  for mature plate boundaries, especially some subduction megathrusts (e.g., Bouchon *et al.*, 2013) and on oceanic transform faults (McGuire *et al.*, 2005).

Although previous studies of foreshocks analyzed seismicity in the days to weeks before M > 6 earthquakes (e.g., Dodge et al., 1996; Felzer et al., 2002; Kato et al., 2012; Yoon et al., 2019), we study only 16 hr time windows prior to M 2.5–3 aftershocks and focus our study on a 2 km sized box surrounding each of those events. We chose the 16 hr time window,

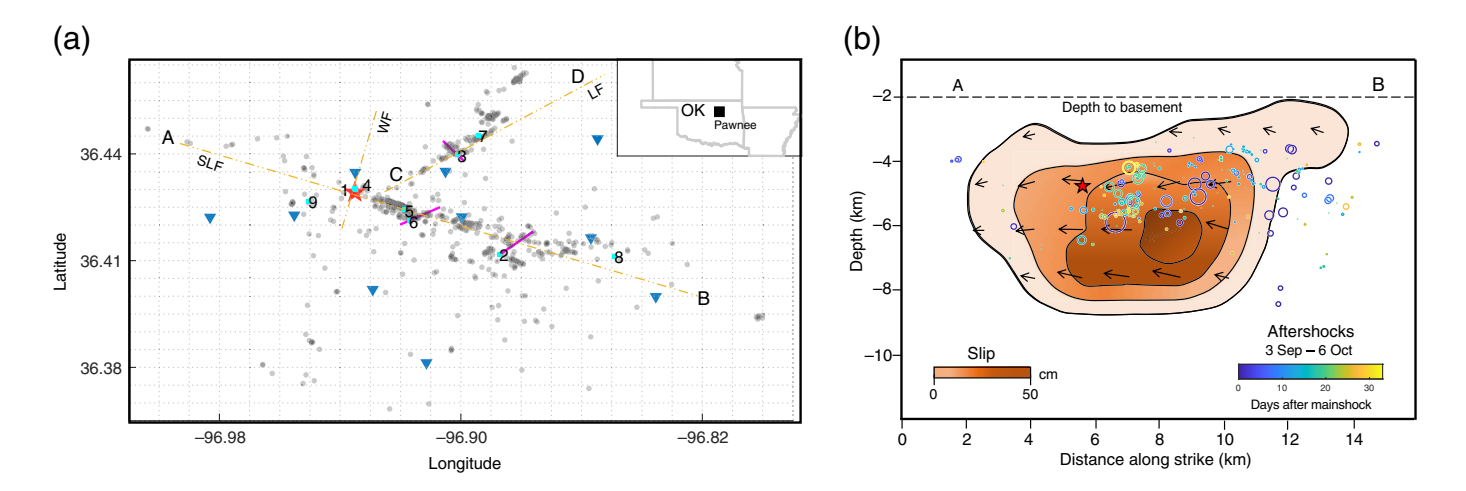
because it is relatively long, compared to the seconds-tominutes event interactions observed during some sequences, but not so long that it is a significant fraction of the time since the mainshock. The 2 km box is approximately twice the radius of influence of an M 2.5 earthquake, as described later.

## **Pawnee Earthquake**

North-central Oklahoma experienced a rapid increase in the number of earthquakes since 2009. The majority of this increased activity is linked to wastewater injection into the Arbuckle Group (e.g., Ellsworth, 2013; Keranen *et al.*, 2013, 2014). Earthquakes generally occur in the basement, and do not associate with known faults compiled via reflection seismic data and geologic mapping (Marsh and Holland, 2016; Schoenball *et al.*, 2018). Rather, they map out faults that show a pattern of conjugate faulting that are favorably aligned for slip within the contemporary tectonic stress state, determined by wellbore measurements to have a maximum horizontal stress  $S_{H\, max}$  of N85°E (Alt and Zoback, 2017).

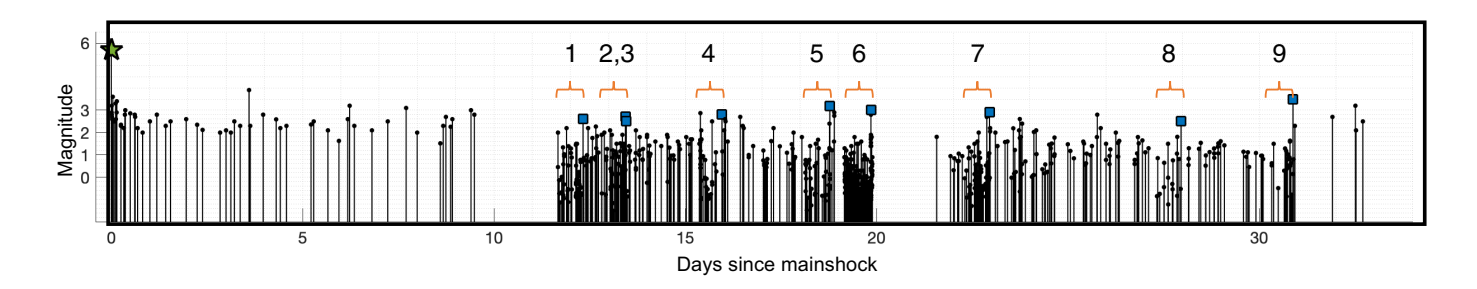
The 2016 September 3 12:02 UTC  $M_{\rm w}$  5.8 Pawnee earthquake occurred as the result of shallow strike-slip faulting about 15 km northwest of Pawnee, Oklahoma. It is the largest instrumentally recorded earthquake in the history of Oklahoma, and was widely felt throughout Oklahoma and neighboring states (USGS, 2016). Figure 1 shows the relevant faults, seismic stations, and located seismicity in our study. The earthquake occurred along the previously unmapped, northwest-southeast-trending Sooner Lake fault (SLF), also known as the Pawnee fault, which crosses the northeast-southwest-trending Labette fault (LF). Both the faults are preferentially aligned for failure in the contemporary stress state (Alt and Zoback, 2017). The SLF also crosses the Watchorn fault, which is apparently inactive and does not host seismicity. From the relocated aftershocks, we observe that the SLF is formed by an en echelon pattern of smaller faults, such as those highlighted near study events 2, 3, and 6. We discuss those in more detail in the Results section. En echelon patterns of fractures had also been observed near the Arkansas River through geological surveys, near the epicenter of the Pawnee mainshock (Kolawole et al., 2017; Schoenball and Ellsworth, 2017). Moment tensors derived by inverting the W phase and regional surface waves indicate left-lateral strike-slip focal mechanisms with near-vertical nodal planes (e.g., Yeck et al., 2017; USGS, 2016).

Figure 1b shows our catalog overlaid on a slip model of the Pawnee earthquake derived from joint kinematic inversion of geodetic and seismological data of Grandin *et al.* (2017). The hypocenter is located in the Precambrian basement at a depth of 4.6 km. The aftershocks roughly delineate the upper edge of the main slip area. They are located within the crystalline basement along a  $\sim$ 7.5 km long segment between 4 and 6 km depth. According to the slip model by Grandin *et al.*, (2017), the rupture was confined within the basement, concentrated in an



**Figure 1.** Relocated seismicity from 3 September to 6 October 2016. (a) Inset map of the location of the study area within Oklahoma. Gray dots describe the relocated seismicity, orange dashed lines denote the three fault traces. LF, Labette fault; SLF, Sooner Lake fault; and WF, Watchorn fault (inactive); the red star is the epicenter of the Pawnee mainshock; inverted triangles are the PW seismic stations; small cyan squares are the nine study events, indexed

chronologically from 1 to 9; magenta lines indicate conjugate subfaults on which study events 2, 3, and 6 lie (b) depth profile of seismicity along AB. Circles are hypocenters with colors indicating the time of each event relative to the mainshock. The background is adapted from the slip model from Grandin *et al.* (2017), derived from the combination of geodetic and seismic datasets. The color version of this figure is available only in the electronic edition.



**Figure 2.** A stem graph of magnitude versus time for the Pawnee earthquake aftershock sequence. We study the spatial–temporal patterns of seismicity in each of the nine highlighted 16 hr

subsequences. Each subsequence leads to an event with  ${\bf M}$  2.5 or above, indicated by blue squares. The color version of this figure is available only in the electronic edition.

8 km long rupture area at 4–9 km depth, and failed to enter the sedimentary layer.

Past research on the Pawnee earthquake has been summarized by Chen and Nakata (2017) and references therein, focusing on the hydrological responses, imaging the rupture process and surface deformation using geodetic and seismic observations, liquefaction, Coulomb stress interactions between the foreshocks and mainshock, and stress drop variations.

### **Methods**

#### Catalog and nine study events

We studied aftershocks in the first 34 days after the Pawnee earthquake to search for candidate M > 2.5 events for more detailed analysis. Excluding events in the first 10 days immediately following the mainshock (which had very high background seismicity) and events that were further than 1 km

from either the SLF or LF, we found nine M > 2.5 events (hereafter "study events"). Figure 2 describes the timing and magnitude of those nine study events. The supplemental text S4, available in the supplemental material to this article, contains the full catalog.

Figure 3 summarizes the magnitude distribution of nine subcatalogs compiled for the nine study events. Each subcatalog is confined both spatially and temporally, containing seismicity in a 2 km  $\times$  2 km box centered around the study event in a 16 hr time window immediately preceding the study event. For catalog number 6, the REST algorithm (Comte *et al.*, 2019) was used to make detections. In the other eight subcatalogs, we chose a reference event of  $\sim$ M 0 located within the 2 km  $\times$  2 km box and then manually searched the entire 16 hr time window for all events with amplitudes greater than or equal to the reference event. Based on this detection procedure, we

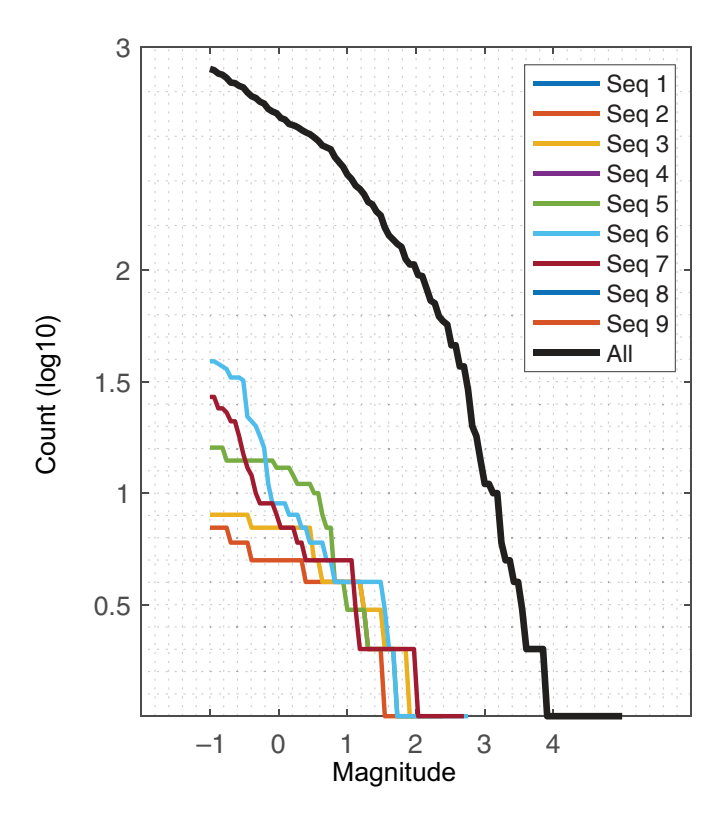


**Figure 3.** Magnitude of completeness. The nine catalogs from the nine study events are complete to  $\mathbf{M}$  0, except sequence 6, which is likely complete to  $\mathbf{M}$  –1. The overall catalog (in black), used to identify study events, is complete to  $\mathbf{M}$  2.5.

conservatively estimate the magnitude of completeness for all the subcatalogs to be M 0. Sequence 6 is likely complete to about M -1. Additional events were also located through match filtering, as described subsequently.

## Source location and relocation

For initial location, we manually picked P and S arrivals from the PW stations. They were deployed from 4 September 2016 to 16 November 2016 as part of the Incorporated Research Institutions for Seismology (IRIS) XR, O2, and Y7 networks, and were sampled at 250 Hz. In total, there were 5707 and 7735 P and S picks, respectively. On average, each event has 14 picks, with the ratio of P/S picks at 0.8.

After initial locations using Antelope's dbloc program, we carry out hypoDD relocations (Waldhauser and Ellsworth, 2000; Waldhauser, 2001) with differential times from both the catalog and cross correlation. In total, we obtained 297,541 *P*-wave differential times from cross correlation and 22,544 from catalog, and 534,866 *S*-wave differential times from cross correlation and 36,859 from catalog. Overall, the amount of cross correlation derived differential times is a factor of 13 larger than those from catalog. The hypoDD double-difference algorithm iteratively solves for hypocentral variations in a least squares' sense by minimizing the residuals of travel times

between pairs of nearby events recorded at common stations, thus removing bias due to velocity model errors. To obtain error estimates of the relocations, we used the resampling with replacement approach, as discussed in Waldhauser and Ellsworth (2000). We grouped our catalog into subsets of  $\sim$ 100 events and then used singular value decomposition on each subset to obtain formal uncertainty estimates, which are tabulated in the supplemental material, and are shown for all events plotted in the Results section.

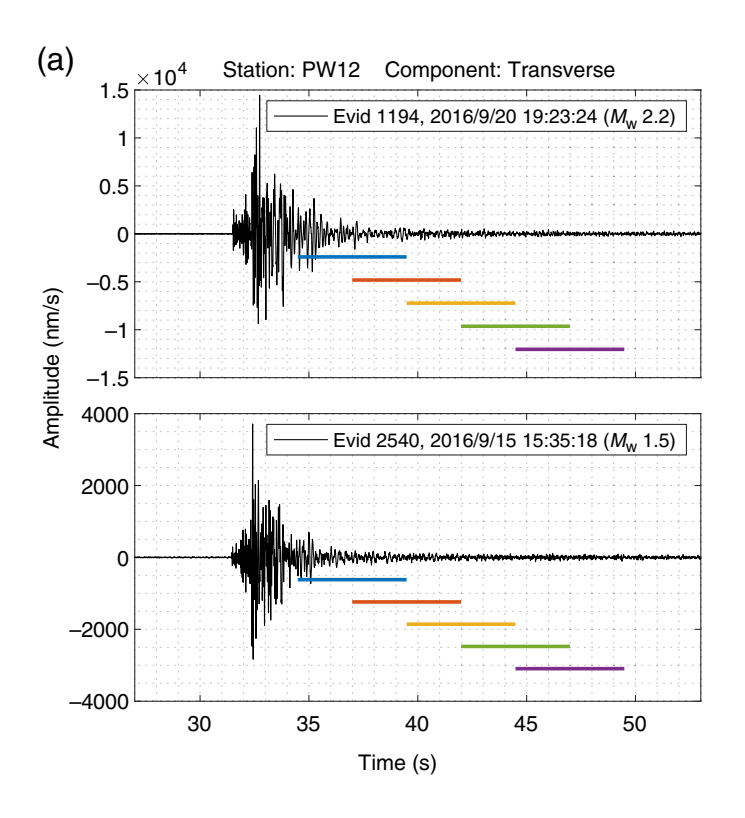
## Match filtering detection

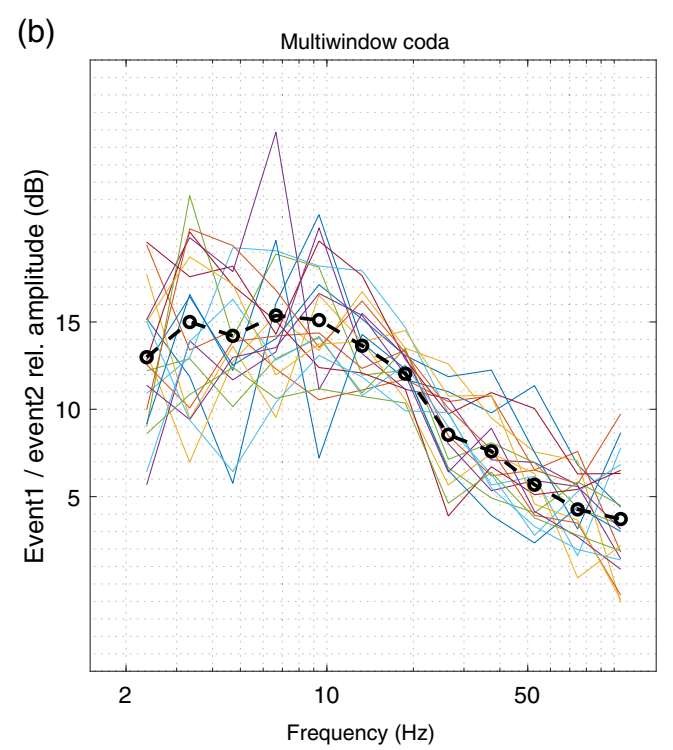
To augment our catalogs, we selected 19 M 1.5–2.5 events that are distributed along the pair of conjugate faults as template events and performed match filtering in the 16 hr window preceding each of the nine study events. In total, 274 additional events were detected. The analysis procedure generally follows that of Shelly *et al.* (2007). Template events were scanned through the continuous waveforms (250 Hz) in hourly blocks for each 16 hr sequence, instead of the entire 24 day record. Templates were cut 1 s before and 5 s after the *P*-wave arrival. Both templates and the continuous waveforms were band-pass filtered between 15 and 24 Hz. Detections occur when the stacked correlation coefficient summed across all stations exceeds eight times the median absolute deviation.

## Spectral ratio analysis to determine magnitude

Event magnitude was determined using the multiwindow coda spectral ratio (MWCSR) method, which was first proposed by Imanishi and Ellsworth (2006) and is an extension of the empirical Green's function method (e.g., Mueller, 1985; Ide et al., 2003). This method takes advantage of the averaging property of S-wave coda (e.g., Mayeda et al., 2007) and has been shown to lead to more stable spectral ratios compared with conventional spectral ratio methods (e.g., Wu et al., 2018). We used three-component velocity seismograms, rotated them to radial, transverse, and vertical directions, and used only the transverse component. For a pair of collocated events, we first calculated the spectral ratios between the larger and the smaller events. We calculated spectral ratios using multiple coda windows and then stacked them. The stacked ratios more closely resemble the theoretical spectral ratio for the omega-squared model (Brune, 1970) than the individual spectra. This is because the cancellation of path effects even for earthquakes at nearly the same location is not exact, and multiple windows suppress the uncorrelated noise introduced by multipaths between source and receiver.

Figure 4 describes the details of the MWCSR method using a pair of collocated events in our catalog. We fix the number of windows to five, so 20 individual spectral windows contribute to the stack (four stations for this event pair, five windows). The length of the time windows used is 5 s. The first window starts at 80% of the S-wave travel time (arrival time–origin time) after its arrival. Each successive window overlaps the





previous one by half the window length. Spectral estimates of each window (colored lines in Fig. 4b) are averaged using the method outlined in appendix A of Wu and McLaskey (2019), and the final stacked spectral ratio is shown in black.

The ideal spectral ratio  $r(\omega)$  is flat at frequencies below the corner frequency of the larger event (event 1) and above the corner frequency of the smaller event (event 2), and falls off with a decay of the form  $\omega^{-y}$  in between. For relative moment estimation, we utilize only the low-frequency amplitude  $\Omega$ , and we utilize the reported seismic moment of the larger events (Yeck *et al.*, 2017), to determine the moment of the smaller events in our catalog ( $\Omega = M_{0,\text{event1}}/M_{0,\text{event2}}$ ). We estimate that our moment calculations are accurate to a factor of 2 (6 dB).

#### Estimation of radius of influence R

An earthquake rupture imparts stress changes that may promote or inhibit additional ruptures in its vicinity. In this work, we assumed that nearby events are coplanar and estimated the on-fault static stress changes  $\Delta \tau(r)$  solely based on the earthquake magnitude and an assumed stress drop  $\Delta \sigma = 2$  MPa, which was found by Wu *et al.* (2018) to be the median stress drop of 73 aftershocks of the 2016 Pawnee sequence. Given the uncertainties in the fault geometry and difficulties estimating the stress drop of these small-magnitude events, we believe a more sophisticated analysis that considers Coulomb stress changes or includes stress drop calculations is not justified. We did estimate the stress drop of the larger events in our catalog based on corner frequencies estimated using the MWCSR-derived spectra (see the supplemental text S3) and found  $\Delta \sigma = 2$  MPa to be a reasonable assumption.

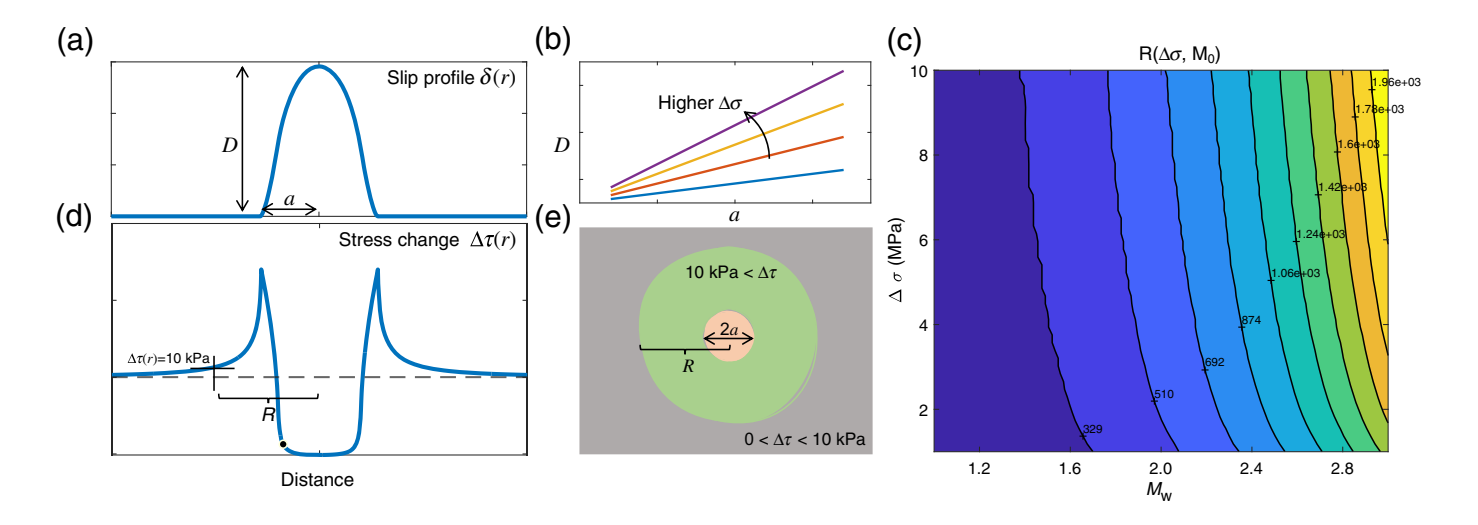
**Figure 4.** Details of the multiwindow coda spectral ratio (MWCSR) method for two collocated events. (a) Transverse component time series with event origin at 30 s. Colored horizontal lines are the windows used in MWCSR. (b) About 20 spectral ratios (four stations  $\times$  five windows) averaged to the final stacked ratio (black). The color version of this figure is available only in the electronic edition.

In our simplified approach, we first estimated the rupture radius a of each event using its seismic moment  $M_0$ , and assume a circular source and  $\Delta\sigma=2$  MPa. Using the expressions for seismic moment  $M_0=GA\bar{D}$  (Aki, 1966) and static stress drop  $\Delta\sigma=\frac{7\pi}{16}G\frac{\bar{D}}{a}$  (Kanamori and Anderson, 1975), we find

$$a = \left(\frac{7}{16} \frac{M_0}{\Delta \sigma}\right)^{\frac{1}{3}},\tag{2}$$

in which G = 30 GPa is the assumed shear modulus,  $A = \pi a^2$  is the rupture area,  $\frac{7\pi}{16}$  is the nondimensional shape factor for circular faults (Eshelby, 1957), and  $\bar{D}$  is the average slip over the rupture area.

We then assign an analytical slip profile  $\delta(r)$  to an event constrained by its a and  $M_0$ , and use it to estimate the onfault stress change  $\Delta \tau(r)$ . We chose the slip profile proposed by Ke et al. (2021) over alternatives (Burridge and Halliday, 1971; Cowie and Scholz, 1992; Bürgmann et al., 1994), because it features a nearly constant stress drop within the ruptured region and stress changes with no singularities (Fig. 5a). For this profile, the ratio between peak slip D and a is fixed for a given



stress drop  $\Delta\sigma$ :  $D=(\frac{p_1}{G}\Delta\sigma)a$ , in which  $p_1=1.55$  and G is assumed to be 30 GPa (Fig. 5b). We compute  $\Delta\tau(r)$  associated with  $\delta(r)$  using a dislocation model (Bilby and Eshelby, 1968) where the stress along the fault plane is expressed in terms of slip (Fig. 5d):

$$\Delta \tau(r,t) = \frac{G}{2\pi(1-\nu)} \int_0^L \frac{\partial \delta(\xi,t)}{(r-\xi)\partial \xi} d\xi, \tag{3}$$

in which  $\nu=0.25$  is the Poisson ratio.  $\Delta\tau(r)$  shows a reduction in shear stress within most of its source radius, an increase near the tip of the arrested rupture, and rapid decay outside the ruptured region (Fig. 5d), as observed in recent laboratory experiments (Ke *et al.*, 2021).

Next, we propose a quantity named "radius of influence" R to characterize the extent of influence for an event. Studies of stress transfer and earthquake triggering suggest that a specific stress threshold for earthquake triggering may not exist (Ziv and Rubin, 2000), rather, stress changes may advance or delay the time of a future nearby earthquake by an amount of time proportional to the amplitude of the stress changes, as well as other factors (Dieterich, 1994). Our work supports this idea and shows that larger stress changes tended to trigger earthquakes in a shorter amount of time. However, to provide a reference line that illustrates an earthquake's stress changes, we assume a 10 kPa threshold for calculating R. 10 kPa is near the lower limit of where correlation between stress changes and seismicity rate changes were observed in many aftershock studies (Harris, 1998; Ziv and Rubin, 2000; and references therein). For  $\Delta \sigma = 2$  MPa stress drop and the 10 kPa threshold R = 8.8a. R is quite sensitive to the choice of threshold; a change to 1 kPa (R > 25a) or 100 kPa  $(R \approx 3a)$  would significantly affect how an event's influence is visualized. However, R is not sensitive to the choice of slip profile. The model of Burridge and Halliday (1971), for example, produces nearly identical stress changes  $\Delta \tau(r)$  for r > 4a.

*R* scales with  $\Delta \sigma$  and  $M_0$ , following a power law relationship (Fig. 5c),

**Figure 5.** Source parameters— $\delta(r)$ ,  $\Delta\tau(r)$ , R. (a) Analytical slip profile  $\delta(r)$ , determined as a function of a and D following Ke et~al., (2021) (b) D and a follow a linear relationship for a given  $\Delta\sigma$ . The equation is given in the Estimation of Radius of Influence R section. (c) Contour plot of R as a function of R and R (d) Stress change profile computed from R (R) using equation (3). Black dashed line is R = 0. The radius of influence R is defined for ranges that satisfy R = 10 kPa. (e) Schematic showing the radius of influence R and R is in green, from the center of the rupture radius until when R = 10 kPa (gray). The color version of this figure is available only in the electronic edition.

$$R(M_0, \Delta \sigma) = c_1 M_0^{\alpha} \Delta \sigma^{\beta}, \tag{4}$$

in which  $c_1 = 5.95 \times 10^{-3} \text{ m} * N^{-1/2}$ ,  $\alpha = 1/3$ ,  $\beta = 1/6$ .

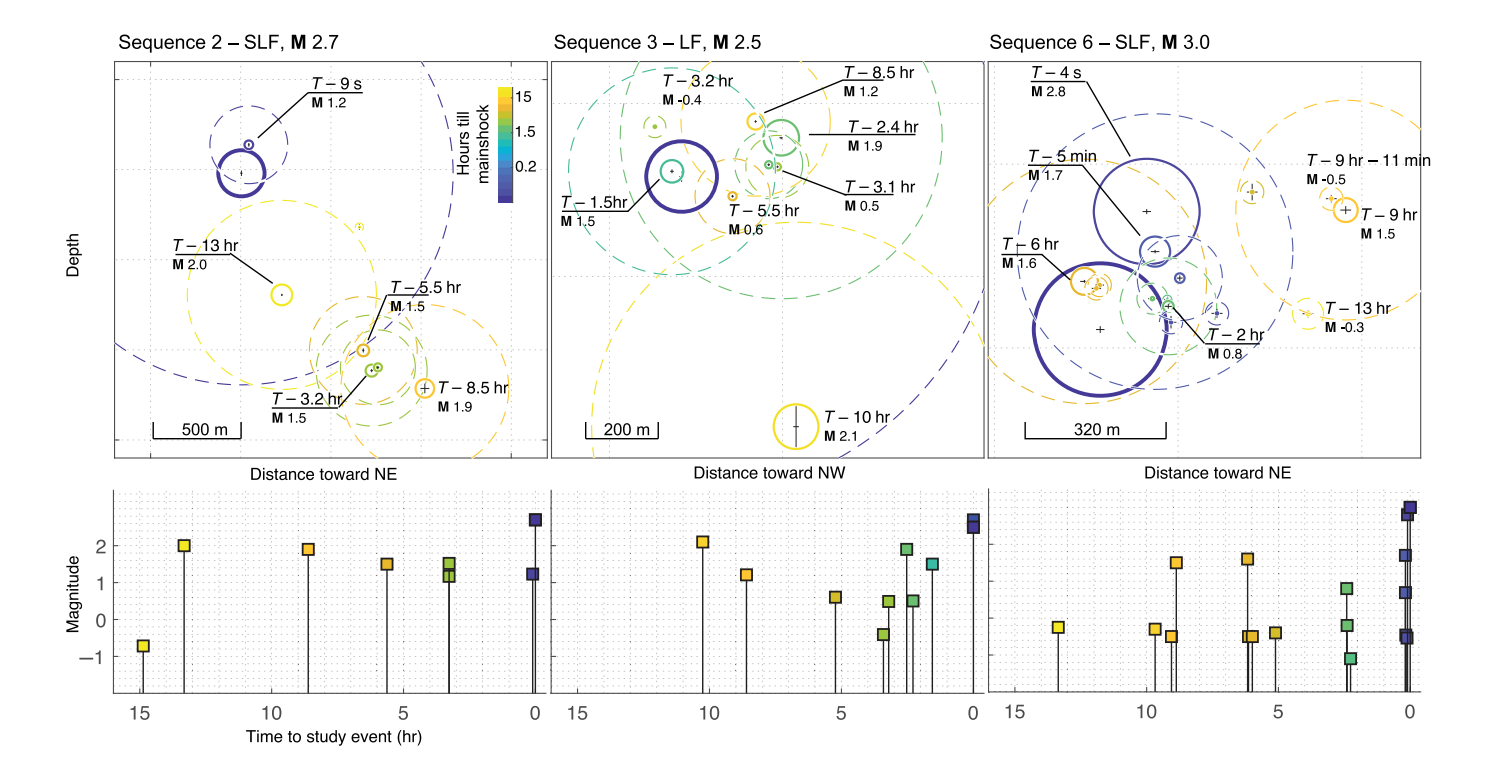
 $M_0$  has far more influence on R than  $\Delta\sigma$ : our 2× (6 dB) uncertainty in  $M_0$ , described earlier, results in ~26% (2 dB) variation in R, whereas a 4× variation in  $\Delta\sigma$  would produce similar variation in R. For this reason, and because  $\Delta\sigma$  estimates depend strongly on corner frequency estimates that are less reliable, we focus our efforts on accurate estimation of  $M_0$  and do not attempt to estimate  $\Delta\sigma$ .

We illustrate the source parameter calculations (a, D, and R) with an M 2.7 event. Given its seismic moment and assuming  $\Delta \sigma = 2$  MPa and a circular rupture, we find through equation (2) that the rupture radius a = 145 m. For the chosen slip profile (Ke *et al.*, 2021) and 2 MPa stress drop assumption, the peak slip D and a are linearly related ( $D = 1.03 \times 10^{-4} a$ ), so D = 15 mm. Next, equation (3) is used to solve for the stress change profile  $\Delta \tau (r, t)$ , which results in R = 1275 m (i.e.,  $\Delta \tau$  drops to 10 kPa at 1275 m from the center of rupture).

#### Results

## Analysis of the nine study sequences

For each event in each of the nine sequences, we compute its R using equation (4) while assuming  $\Delta \sigma = 2$  MPa. We then plot the event hypocenters, estimated rupture areas, and radii of influence (assuming a 10 kPa threshold) projected onto a fault



plane (Figs. 6, 7, and Fig. S1). For sequences 5 and 7, the relevant events roughly lie on the SLF and LF, respectively. However, the relevant events for sequences 2, 3, and 6 scatter along subfaults that are conjugate to the SLF and LF whose orientations are described in Figure 1. Figure 6 shows the spatiotemporal patterns of seismicity for sequences 2, 3, and 6 with the events projected onto their respective conjugate subfaults. Figure 7 shows sequences 5 and 7 with relevant events projected onto the SLF and LF, respectively, as well as zoom-ins of some smaller swarms that occurred within the 16 hr time window. Figures 6 and 7 also contain stem graphs of magnitude against time until the study event, similar to Figure 2. Sequences 1, 4, 8, and 9 have no observable prior events within the spatiotemporal constraints and, therefore, are only shown in Figure S1. Because of their close proximity in space and time, sequences 5 and 6 may be linked; however, because they appear to occur on different subfaults and are separated by more than 16 hr, we consider them separately.

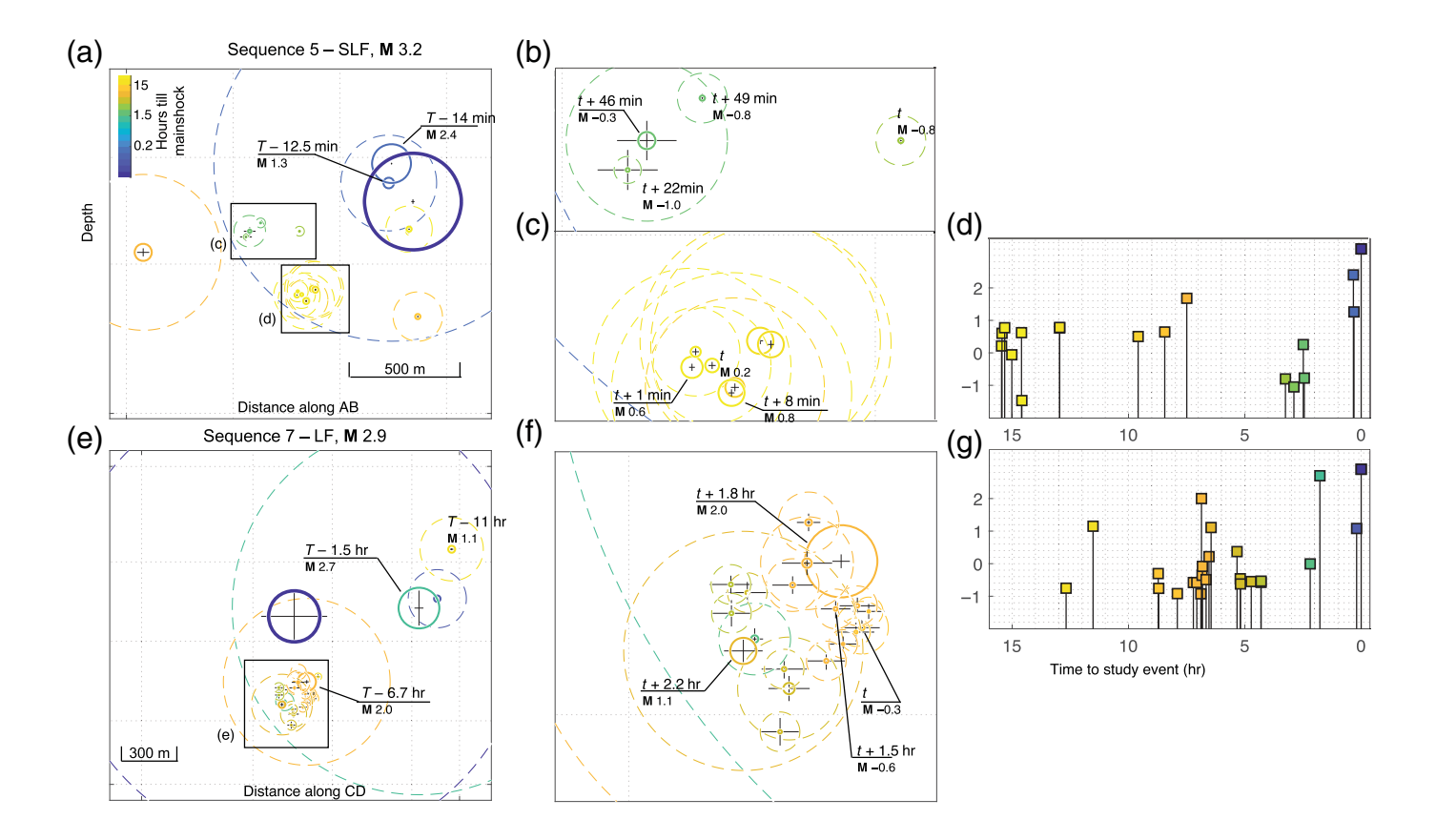
**Sequences 2, 3, and 6.** In sequence 2, an M 1.2 event occurred 9 s prior to the M 2.7 study event (i.e. "T-9 s"). The radius of influence of that event overlaps with the hypocenter of the study event, so we believe that the M 2.7 study event was triggered through standard stress transfer. In the lower right corner, an M 1.9 event 8.5 hr prior to the study event triggered two M 1.5 events 3 and 5 hr later, respectively. However, the M 2.0 and 1.2 events have no preceding triggering events within the 16 hr time window.

Sequence 3 started with two events of M 2.1 (T = 10 hr) and M 1.2 (T = 8.5 hr) with no immediately preceding triggering

**Figure 6.** Sequences 2, 3, and 6. For each sequence, the estimated rupture areas of prior events are plotted as solid circles, and the study event is bolder and in bold blue; the rupture radius is computed using equation (2) for  $\Delta \sigma = 2$  MPa. The timing of the relevant events are labeled as T – <time till study event>. The dashed lines are the radii of influence computed using equation (4), plotted in the same color as the event itself. Sequences 3 and 6 have been zoomed in to better show the details. Black crosses show uncertainty in event locations and span from, for example, -dz to +dz, in which dz is the error estimate reported in supplemental file S4. On the bottom panel, we plot stem graphs of magnitude versus time for relevant events of the three sequences, which are color coded with the top panel.

events. After the M 1.2, event, three events follow in a cascading manner (M 0.6, -0.4, and 0.5), with the first two only slightly outside of the radius of influence of the triggering M 1.2 event. The last of the three (M 0.5) triggered an M 1.9 event (T = 2.4 hr), which then triggered the remaining events (including the one not labeled), all through standard stress transfer consistent with the cascade model.

Sequence 6 started with two events of  $\mathbf{M}$  –0.3 (T = 13 hr) and  $\mathbf{M}$  –0.5 (T = 9 hr–11 min), with no immediately preceding events. The latter seemed to trigger an  $\mathbf{M}$  1.5 event 11 min later, although its R does not fully extend to the hypocenter of the  $\mathbf{M}$  1.5 event. Three hours later, an  $\mathbf{M}$  1.6 event occurred without preceding triggering events. It triggered a sequence of events ( $\mathbf{M}$  0.8 T = 2 hr,  $\mathbf{M}$  1.7 T = 5 min,  $\mathbf{M}$  2.8 T = 4 s) that eventually led to the study event, all through standard stress transfer consistent with the cascade model.



**Sequences 5 and 7.** In sequence 5, shown in Figure 7, an M 2.4 event occurred 14 min prior to the M 3.2 study event. In sequence 7, an M 2.7 event occurred 1.5 hr prior to the M 2.9 study event. In both the cases, the radius of influence of the preceding events (M 2.4 and 2.7) overlaps with the hypocenters of the study events, so we believe that the two study events were triggered through standard stress transfer.

Sequences 5 and 7 both contain swarms of seismicity that call for more scrutiny, because swarms can be indicative of aseismic forcing. In sequence 5, there were two swarms of seismicity that are 1.5 and 15 hr before the study event. The  ${\bf M}$  0 events that compose the swarms have more limited radius of influence and likely do not affect the cascading sequence that starts around T=14 min. However, it is worth zooming in to observe how each swarm develops.

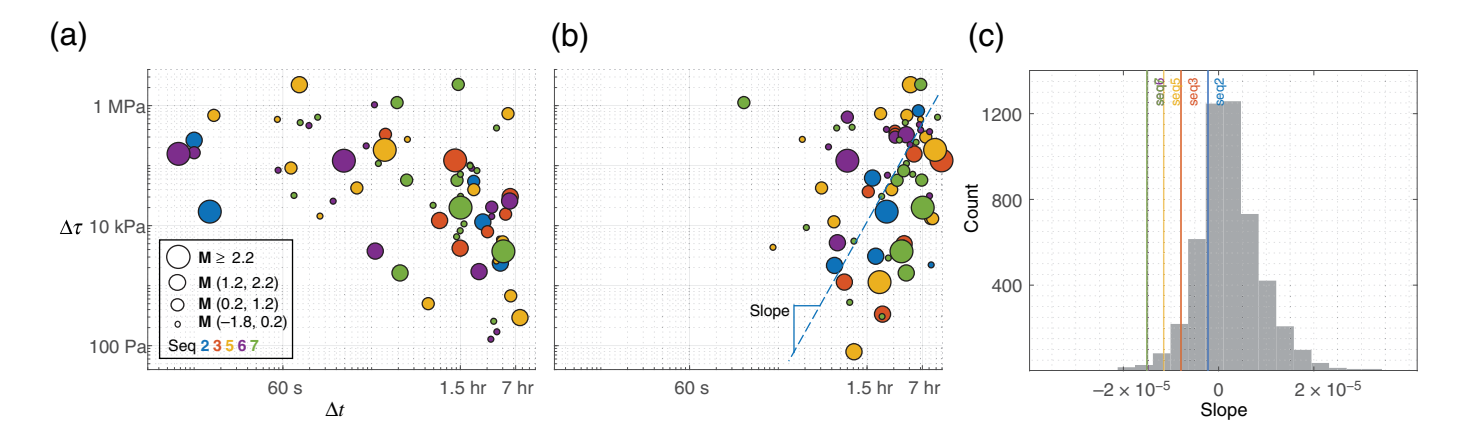
To better describe the relative timing of the swarm events, we denote the first event as occurring at time "t," and the subsequent events are at " $t + \Delta t$ ". Swarm (c) consists of four events, and three of them cannot be easily explained by standard stress transfer. The sequence starts with an  $\mathbf{M}$  –0.8 event, followed by  $\mathbf{M}$  –1.0 (t + 22 min) and  $\mathbf{M}$  –0.3 (t + 46 min), and finally another  $\mathbf{M}$  –0.8 (t + 49 min). It is unlikely that the first three events triggered each other via static stress transfer. Their radii of influence are too small compared to the spatial separation of their hypocenters. This type of behavior may suggest some ~100 m scale aseismic process that triggered the first three events of the swarm. Approximately 100 m scale slow fault slip would be inconsistent with the cascade model. The

**Figure 7.** Sequences 5 and 7 and their swarms. As in Figure 6, the rupture areas, radii of influence, and location uncertainties are plotted as solid circles, dashed circles, and black crosses, respectively. The study event is bold blue, and the timing of the relevant events relative to the study event is labeled. (b,c,f) Zoomins of the boxed regions in (a) and (e). (d,g) Color-coded stem graphs of magnitude versus time for the sequences shown in (a) and (e), respectively.

last event of the swarm ( $\mathbf{M}$  –0.8 at t + 49 min) falls within the radius of influence of the preceding  $\mathbf{M}$  –0.3 event and can be easily explained as an aftershock of the  $\mathbf{M}$  –0.3.

Swarm (d) consists of seven events and only the first (M 0.2) cannot be easily explained by standard stress transfer. Two events of M 0.6 (t+1 min), M 0.8 (t+8 min) followed the first event in standard cascading fashion. The hypocenters of all the following events in a 2.5 hr window fall within the radius of influence of the M 0.8 event and, therefore, were triggered through static stress transfer.

In swarm (e) of sequence 7, we only highlight the time and magnitude of the relevant events. Three events cannot be easily explained by standard stress transfer: the first event ( $\mathbf{M}$  –0.3), an  $\mathbf{M}$  –0.6 event (t + 1.5 hr) that falls slightly out of the radius of influence of the first event and the  $\mathbf{M}$  2.0 event whose hypocenter also falls somewhat out of the radius of influence of the first two events. All the remaining, unlabeled events that followed fall within the influence of the  $\mathbf{M}$  2.0 and 1.1 events and, therefore, were likely triggered through static stress transfer,



consistent with the cascade model. We omitted their labels for clarity. The **M** 2.7 event (T = 1.5 hr) also falls somewhat outside the radius of influence of the **M** 2.0 (T = 6.7 hr).

**Sequences 1, 4, 8, and 9—No foreshocks.** Study events 1, 4, 8, and 9 had no events ( $M \ge 0$ ) in their vicinity within the 16 hr time window.

## Summary of spatiotemporal triggering

Figure 8a summarizes the seismicity of sequences 2, 3, 5, 6, and 7 by plotting, for each event of each sequence, the time elapsed since its likely triggering event ( $\Delta t$ ) and the estimated stress change  $(\Delta \tau)$  imparted by the triggering event. When an event could have multiple potential triggering events, we picked the one that would result in the largest  $\Delta \tau$ . The first event of each sequence is omitted because  $\Delta t$  is undefined. The figure shows that short triggering times ( $\Delta t$  < 6 min) were always associated with  $\Delta \tau > 10$  kPa. Out of 71 events in the five sequences, 50 events (70%), including all five study events, fall above the 10 kPa threshold. The other events apparently triggered by  $\Delta \tau < 10$  kPa are those that are more difficult to explain with standard stress transfer from immediately preceding events. As discussed earlier, some isolated events can be explained as resulting from stress perturbations from the Pawnee mainshock; however, sequence 5 contained a number of prior earthquakes that occurred far outside the radii of influence of immediately preceding events, suggesting that perhaps some ~100 m scale aseismic process was responsible for triggering some of the earthquakes, or that our assumptions about triggering due to standard stress transfer are not entirely appropriate. The events of sequence 5 were generally aligned with the SLF, which ruptured in the M 5.8 Pawnee mainshock, so it is possible that afterslip on this fault was responsible. The other events prior to other study events were aligned either with the conjugate LF or smaller conjugate faults.

For all five sequences, we observe an inverse relationship between  $\Delta \tau$  and  $\Delta t$  for the larger events (M > 1.2). This suggests that while small  $\Delta \tau < 10$  kPa can potentially trigger an earthquake, the triggering process takes more time if  $\Delta \tau$  is small. This is consistent with a time-dependent nucleation

**Figure 8.** Summary of sequences 2, 3, 5, 6, and 7. (a) For each event,  $\Delta \tau$  is the stress change imparted by its assumed triggering event, and  $\Delta t$  is the time lapse between them. The first event of each sequence is omitted. The size of the circle denotes the magnitude of each event, and the color indicates the sequence to which it belongs. (b) An example of time-randomized catalog. The dashed line shows the least squares fit for sequence 2. (c) The histogram shows the slope of 1000 randomized catalogs. Each vertical line indicates the actual slope of a sequence.

process that is a function of  $\Delta \tau$  (e.g., Dieterich, 1994). On the other hand, quasi-static afterslip (known to occur after many earthquakes) would also produce a time-variable effect, as would other anelastic responses of the rock mass.

#### Limitations

Our analysis of triggering and stress transfer relies on a number of simplifying assumptions. We assume circular ruptures with radial rupture propagation such that the earthquake hypocenter is also its centroid. Unilateral and noncircular earthquake ruptures are commonly observed, and this could produce location errors as large as 1-2a (<23% variations in R, for our 10 kPa threshold). We also assumed a stress drop  $\Delta \sigma = 2$  MPa when calculating the radius of influence R. About  $10\times$  variations in  $\Delta\sigma$  would cause  $\sim$ 50% variations in R. Our estimates of moment may be uncertain by up to  $2\times$ , which would cause  $\sim$ 30% variation in R. As previously mentioned, a  $10\times$  change in triggering threshold (i.e., 100 kPa or 1 kPa) would cause the most significant variations in R ( $3\times$  or 300%).

Second, our simplification of stress changes shown in Figures 5 and 6 are only strictly accurate when both triggered and triggering earthquakes occur on the same planar fault. In reality, earthquakes may occur in a more complicated damage zone. This geometrical effect, as well as the effect of varied focal mechanisms of the earthquakes, would produce more complicated stress changes, including changes in both normal stress and shear stress (e.g., King et al., 1994) that are not taken into account in this study.

## **Randomized Catalogs**

In this section, we explore the extent to which our findings of prior seismicity could be due to chance. If we were studying earthquakes that occurred randomly in space and time, would we have reached the same conclusions? As described in the previous section, those conclusions are: inverse relationship between  $\Delta \tau$  and  $\Delta t$ , and four out of nine study events without any precursors within the spatiotemporal constraints.

To check this, we first randomized the event timing. For each event in each of the five sequences shown in Figures 6 and 7 (except the study event), we drew the event time from a uniform distribution from 0 to 16 hr while keeping its location unchanged.  $\Delta t$  and  $\Delta \tau$  were then computed using the method described in the Results section. About 1000 such time-randomized catalogs were generated, with an example shown in Figure 8b. Data points in the randomized catalogs were uniformly distributed in time, but when plotted on a log time scale they appear to be concentrated at higher values of  $\Delta t$  compared to the sequences shown in Figure 8a.

In Figure 8c, we quantitatively show the difference between the actual catalogs and the time-randomized ones by comparing their slopes in log space. We assume a power law relationship between  $\Delta \tau$  and  $\Delta t$  (e.g., Dieterich, 1994)  $\Delta \tau \propto \Delta t^n$ , and compute the exponent n via linear regression between  $\log(\Delta \tau)$  and  $\log(\Delta t)$  for each sequence in each time-randomized catalog. A histogram of all slopes n is shown in Figure 8c. After converting the histogram into a cumulative distribution function, we find that the slope values of the five sequences ranked in the 21st, 5th, 2nd, 1st, and 1st percentiles of all simulated catalogs. This indicates that the characteristics we find in Figure 8a are not due to chance. We also generated location-randomized catalogs, which showed that four out of nine study events without prior seismicity was also unlikely due to chance (supplemental text S2).

#### Discussion

As described in the Introduction, the direct application of laboratory friction values suggests a small  $h^*$  ( $\sim$ 1 m), but if the lab values should be scaled up to match the conditions of natural faults (i.e., increased roughness) we could expect a large  $h^*$  (>1 km). The dimension of small earthquakes may place an upper bound on  $h^*$ , except that fault heterogeneity might significantly complicate this interpretation. The smallest earthquake we could quantitatively study is M -1.5, and sequence 6 may be complete down to M -1. Assuming a circular rupture and  $\Delta \sigma = 2$  MPa, an M -1.0 event has a rupture radius of a = 2.0 m. This naively places the upper bound of  $h^*$  to be  $\sim$ 1 m, consistent with laboratory expectations. This small  $h^*$  implies that both M-1 and 3 earthquakes initiate similarly, just the M-1 event arrested, whereas the M 3 event saw fault conditions favorable for continued rupture.

With a small  $h^*$  ( $\sim$ 1 m), the spatiotemporal clustering of events observed prior to five of the nine study sequences is most easily explained as triggering due to standard stress

transfer. The majority of the events studied in this work corroborate with this interpretation, as long as 10 kPa can be considered a reasonable stress perturbation for triggering earthquakes within minutes to hours.

If  $h^*$  were actually on the order of 1 km, and larger events nucleated following a classical self-nucleation processes consistent with modeling studies (Dieterich, 1992) and laboratory experiments (McLaskey and Kilgore, 2013), then we might expect to see an acceleration of the rate of seismicity as the time to a nucleating event nears as well as a migration of seismicity (over hundreds of meters) with the expansion of the nucleation-related slow slipping region. We do observe clusters of activity and minutes-long to seconds-long periods of elevated seismic activity prior to some of the study events, but clear evidence of acceleration or migration is lacking.

The four study events without detectable prior seismicity do not constrain  $h^*$  but offer clues to the variability in fault conditions. If  $h^*$  was small, the "no foreshock" scenario could be interpreted as an extreme manifestation of the cascade model. Instead of a sequence of events that trigger each other through stress transfer until one event grows into a large rupture, the very first detectable event occurred at a location with favorable stress conditions that allowed it to grow into a larger rupture. If  $h^*$  was large, the "no foreshock" scenario would simply suggest that heterogeneity was mild enough that any events driven by nucleation-related slow slip were too small or slow to be detected. In either case, the "no foreshock" scenario implies a lack of heterogeneity in fault properties—a lack of fault conditions required for events to both initiate and terminate. Yet the seismicity observed in the other five sequences indicates that, for those times and locations, there was ample heterogeneity for many smaller events to initiate and terminate without growing large. This contrast implicates strong variability of fault properties even within our 15 km study region in north-central Oklahoma.

Overall, our observations of small-magnitude events and spatiotemporal clustering are consistent with a meter-sized  $h^*$  and a cascade foreshock model, and inconsistent with a classical self-nucleation process with a kilometer-sized  $h^*$ , but they cannot completely rule out more complicated scenarios that include interactions between large slow slipping regions and small events generated by the localized reduction in  $h^*$ . For example, Cattania and Segall (2021) presented models that illustrate how heterogeneous fault conditions can produce sequences of foreshocks with spatiotemporal clustering consistent with triggering due to stress transfer, yet the foreshocks are both driven by and contribute to aseismic slip. Such a scenario exemplifies how it is difficult to distinguish between different earthquake nucleation models by spatiotemporal patterns alone, except for extreme cases, such as repeating earthquakes that are true rerupture of the same fault patch (presumably driven by aseismic slip) or events that are so distant compared to their size that triggering from static stress transfer is very unlikely.

Another complicating factor is that our entire study area was perturbed (>10 kPa) by the M 5.8 Pawnee earthquake, which occurred 12-30 days earlier. This is the likely cause of isolated events that do not fall within the radius of influence of any preceding events in the 16 hr windows, but we might also expect pervasive aseismic afterslip or some other stress relaxation process associated with the Pawnee mainshock. If afterslip is an important driver of the seismicity, then the events we observe might be the isolated rupture of the most unstable or most highly coupled sections of the faults that are loaded by the slow slip of the surrounding, more stable fault sections. In such a case, stress triggering and spatiotemporal clustering could still occur, as described by the Cattania and Segall (2021) model, but it may not be the dominant driver of seismicity. However, the conjugate faults defined by many of the earthquake locations would complicate the afterslip scenario.

#### Conclusion

We studied seismicity in 16 hr time windows leading up to nine study events that are M 2.5–3.0 aftershocks of the 3 September 2016 M 5.8 Pawnee earthquake. We estimated the static stress changes associated with each event of each sequence based on the magnitude and an assumed 2 MPa stress drop. We then defined each event's radius of influence using a 10 kPa stress change as the cutoff and used that to guide whether subsequent events were triggered through static stress transfer or whether they occurred so far outside the radius of influence that aseismic slip or some other triggering process should be implicated.

As summarized in Figure 8a, 70% of the events studied occurred within the radius of influence of a prior event, assuming a 10 kPa cutoff, and were, therefore, likely triggered through standard stress transfer. We also found that rapid triggering, with less than 6 min of time delay between the triggering and triggered events, was always the result of >10 kPa stress changes. However, some clusters of events appear to have been triggered with <10 kPa stress changes, particularly in sequence 5, whose events were aligned with the SLF. This may be an indication of afterslip-triggered seismicity. Of the remaining eight study events, four showed foreshock sequences where the vast majority of the events could be explained through standard stress transfer, consistent with the cascade model, without any requirement for extended aseismic preslip. The other four sequences did not have any detectable seismicity within a 2 km radius of their hypocenters in the preceding 16 hr time windows. Such conditions indicate a lack of strong heterogeneity in fault stress and strength, but the contrast with the other five sequences, which did possess the heterogeneity required for prior events to both initiate and terminate, speaks to the strong variability of fault properties that likely exists in this fault system in the crystalline basement below Oklahoma.

When considering the set of nine study events, we argue that the observations favor a small nucleation length scale ( $h^* \le 1$  m)

for seismogenic depths in north-central Oklahoma, consistent with laboratory expectations. Our observations do not favor a kilometer-scale classic self-nucleation in which preslip smoothly accelerates to dynamic instability (e.g., Ohnaka and Kuwahara, 1990; Dieterich, 1992). The existence of small events ( $\mathbf{M}$  –1), with rupture dimensions on the order of 1–2 m suggest  $h^* \leq 1$  m, and likely provides a viable mechanism to circumvent a large preslip nucleation. The spatiotemporal clustering of seismicity described above generally supports a small  $h^*$ ; however, recent modeling studies (Cattania and Segall, 2021) demonstrate that spatiotemporal seismicity patterns alone cannot rule out more complicated earthquake initiation scenarios that involve the interplay between foreshocks and widespread aseismic slip.

#### **Data and Resources**

Seismograms used in this study were collected using Program for the Array Seismic Studies of the Continental Lithosphere (PASSCAL) instruments. Data can be obtained from the Incorporated Research Institutions for Seismology Data Management Center (IRIS DMC) at <a href="https://ds.iris.edu/mda/">https://ds.iris.edu/mda/</a> (last accessed November 2019). All PW stations are listed under the XR, O2, and Y7 networks. The supplemental material contains three additional figures (Figs. S1–S3) and a catalog of all the events studied (Table S4).

## **Declaration of Competing Interests**

The authors acknowledge that there are no conflicts of interest recorded.

## **Acknowledgments**

The authors gratefully acknowledge that this work was funded by National Science Foundation (NSF) Grants EAR-1645163 and EAR-1847139. The authors thank the seismic network operators of the Incorporated Research Institutions for Seismology (IRIS) and Katie Keranen for access to the continuous time series data of the PW broadband stations. Geoff Abers, Nate Stevens, and Michael Mann provided valuable input and assistance. The authors thank Katie Keranen for initial motivation and assistance with analysis of the Oklahoma seismicity. The authors thank Bill Ellsworth and two anonymous reviewers for helpful comments that improved the article.

## References

Abercrombie, R. E., and J. R. Rice (2005). Can observations of earth-quake scaling constrain slip weakening? *Geophys. J. Int.* **162**, 406–424.

Aki, K. (1966). Generation and propagation of G waves from the Niigata earthquake of June 16, 1964: Part 2. Estimation of earthquake moment, released energy, and stress-strain drop from the G wave spectrum, *Bull. Earthq. Res. Inst. Univ. Tokyo* 44, no. 1, 73–88.

Alt, R. C., and M. D. Zoback (2017). In situ stress and active faulting in Oklahoma, *Bull. Seismol. Soc. Am.* **107**, no. 1, 216–228.

Andrews, D. J. (1978). Coupling of energy between tectonic processes and earthquakes, *J. Geophys. Res.* **83**, no. B5, 2259–2264.

Barbot, S., N. Lapusta, and J.-P. Avouac (2012). Under the hood of the earthquake machine: Toward predictive modeling of the seismic cycle, *Science* **336**, no. 6082, 707–710.

- Beroza, G. C., and W. L. Ellsworth (1996). Properties of the seismic nucleation phase, *Tectonophysics* **261**, 209–227.
- Bilby, B. A., and J. D. Eshelby (1968). Dislocations and the theory of fracture, in *Fracture, an Advanced Treatise*, Chap. 2, H. Liebowitz (Editor), Vol. I, Academic, San Diego, California, 99–182.
- Blanpied, M. L., D. A. Lockner, and J. D. Byerlee (1995). Frictional slip of granite at hydrothermal conditions, *J. Geophys. Res.* **100**, no. B7, 13,045–13,064.
- Bouchon, M., V. Durand, D. Marsan, H. Karabulut, and J. Schmittbuhl (2013). The long precursory phase of most large interplate earthquakes, *Nat. Geosci.* **6**, no. 4, 299–302.
- Brune, J. N. (1970). Tectonic stress and the spectra of seismic shear waves from earthquakes, *J. Geophys. Res.* **75**, no. 26, 4997–5009.
- Bürgmann, R., D. D. Pollard, and S. J. Martel (1994). Slip distributions on faults: effects of stress gradients, inelastic deformation, heterogeneous host-rock stiffness, and fault interaction, *J. Struct. Geol.* 16, no. 12, 1675–1690.
- Burridge, R., and G. S. Halliday (1971). Dynamic shear cracks with friction as models for shallow focus earthquakes, *Geophys. J. Roy. Astron. Soc.* **25**, 261–283.
- Carpenter, B. M., C. Marone, and D. M. Saffer (2011). Weakness of the San Andreas Fault revealed by samples from the active fault zone, *Nat. Geosci.* **4**, no. 4, 251–254.
- Cattania, C., and P. Segall (2021). Precursory slow slip and foreshocks on rough faults, *J. Geophys. Res.* **126**, no. 4, e2020JB020430, doi: 10.1029/2020JB020430.
- Chen, X., and N. Nakata (2017). Preface to the focus section on the 3 September 2016 Pawnee, Oklahoma, earthquake, Seismol. Res. Lett. 88, no. 4, 953–955.
- Chen, X., and P. M. Shearer (2013). California foreshock sequences suggest aseismic triggering process, *Geophys. Res. Lett.* 40, no. 11, 2602–2607.
- Comte, D., M. Farias, S. Roecker, and R. Russo (2019). The nature of the subduction wedge in an erosive margin: Insights from the analysis of aftershocks of the 2015 Mw 8.3 Illapel earthquake beneath the Chilean Coastal Range, *Earth Planet. Sci. Lett.* **520**, 50–62.
- Cowie, P. A., and C. H. Scholz (1992). Growth of faults by accumulation of seismic slip, *J. Geophys. Res.* **97**, no. B7, 11,085–11,095.
- Dieterich, J. H. (1992). Earthquake nucleation on faults with rate-and state-dependent strength, *Tectonophysics* **211**, nos. 1/4, 115–134.
- Dieterich, J. H. (1994). A constitutive law for rate of earthquake production and its application to earthquake clustering, *J. Geophys. Res.* **99**, 2601–2618.
- Dodge, D. A., G. C. Beroza, and W. L. Ellsworth (1996). Detailed observations of California foreshock sequences: Implications for the earthquake initiation process, *J. Geophys. Res.* **101**, no. B10, 22,371–22,392.
- Ellsworth, W. L. (2013). Injection-induced earthquakes, *Science* **341**, no. 6142, doi: 10.1126/science.1225942.
- Ellsworth, W. L., and G. C. Beroza (1995). Seismic evidence for an earthquake nucleation phase, *Science* **268**, 851–855.
- Ellsworth, W. L., and F. Bulut (2018). Nucleation of the 1999 Izmit earthquake by a triggered cascade of foreshocks, *Nat. Geosci.* 11, no. 7, 531–535.
- Eshelby, J. D. (1957). The determination of the elastic field of an ellipsoidal inclusion, and related problems, *Proc. Math. Phys. Sci.* **241**, no. 1226, 376–396.

- Felzer, K. R., T. W. Becker, R. E. Abercrombie, G. Ekström, and J. R. Rice (2002). Triggering of the 1999 Mw 7.1 Hector Mine earthquake by aftershocks of the 1992 Mw 7.3 Landers earthquake, *J. Geophys. Res.* 107, no. B9, ESE-6.
- Grandin, R., M. Vallée, and R. Lacassin (2017). Rupture process of the Mw 5.8 Pawnee, Oklahoma, earthquake from Sentinel-1 InSAR and seismological data, Seismol. Res. Lett. 88, no. 4, 994–1004.
- Guérin-Marthe, S., S. Nielsen, R. Bird, S. Giani, and G. Di Toro (2019).
  Earthquake nucleation size: Evidence of loading rate dependence in laboratory faults, *J. Geophys. Res.* 124, no. 1, 689–708, doi: 10.1029/2018JB016803.
- Harris, R. A. (1998). Introduction to special section: Stress triggers, stress shadows, and implications for seismic hazards, *J. Geophys. Res.* **103**, 24,347–24,358.
- Ida, Y. (1972). Cohesive force across the tip of a longitudinal shear crack and Griffith's specific surface energy, J. Geophys. Res. 77, 3796–3805.
- Ide, S., G. C. Beroza, S. G. Prejean, and W. L. Ellsworth (2003). Apparent break in earthquake scaling due to path and site effects on deep borehole recordings, *J. Geophys. Res.* 108, no. B5, doi: 10.1029/2001JB001617.
- Imanishi, K., and W. L. Ellsworth (2006). Source scaling relationships of microearthquakes at Parkfield, CA, determined using the SAFOD pilot hole seismic array, *Earthquakes: Radiated Energy and the Physics of Faulting*, Vol. 170, 81–90.
- Kameda, J., M. Shimizu, K. Ujiie, T. Hirose, M. Ikari, J. Mori, K. Oohashi, and G. Kimura (2015). Pelagic smectite as an important factor in tsunamigenic slip along the Japan Trench, *Geology* 43, no. 2, 155–158.
- Kanamori, H., and D. L. Anderson (1975). Theoretical basis of some empirical relations in seismology, *Bull. Seismol. Soc. Am.* **65**, no. 5, 1073–1095.
- Kaneko, Y., and N. Lapusta (2008). Variability of earthquake nucleation in continuum models of rate-and-state faults and implications for aftershock rates, *J. Geophys. Res.* 113, doi: 10.1029/2007JB005154.
- Kato, A., K. Obara, T. Igarashi, H. Tsuruoka, S. Nakagawa, and N. Hirata (2012). Propagation of slow slip leading up to the 2011 Mw 9.0 Tohoku-Oki earthquake, *Science* 335, no. 6069, 705–708.
- Ke, C. Y., G. C. McLaskey, and D. S. Kammer (2021). The earthquake arrest zone, *Geophys. J. Int.* 224, no. 1, 581–589.
- Keranen, K. M., H. M. Savage, G. A. Abers, and E. S. Cochran (2013).
  Potentially induced earthquakes in Oklahoma, USA: Links between wastewater injection and the 2011 Mw 5.7 earthquake sequence, *Geology* 41, no. 6, 699–702.
- Keranen, K. M., M. Weingarten, G. A. Abers, B. A. Bekins, and S. Ge (2014). Sharp increase in central Oklahoma seismicity since 2008 induced by massive wastewater injection, *Science* 345, no. 6195, 448–451.
- King, G. C., R. S. Stein, and J. Lin (1994). Static stress changes and the triggering of earthquakes, *Bull. Seismol. Soc. Am.* **84**, no. 3, 935–953.
- Kolawole, F., E. A. Atekwana, and A. Ismail (2017). Near-surface electrical resistivity investigation of coseismic liquefactioninduced ground deformation associated with the 2016 Mw5.8 Pawnee, Oklahoma, earthquake, Seismol. Res. Lett. 88, no. 4, 1017–1023.

- Latour, S., A. Schubnel, S. Nielsen, R. Madariaga, and S. Vinciguerra (2013). Characterization of nucleation during laboratory earthquakes, Geophys. Res. Lett. 40, no. 19, 5064-5069.
- Lui, S. K. Y., and N. Lapusta (2016). Repeating microearthquake sequences interact predominantly through postseismic slip, Nat. Commun. 7, no. 1, 1-7.
- Marone, C., and B. Kilgore (1993). Scaling of the critical slip distance for seismic faulting with shear strain in fault zones, Nature 362, 618-621.
- Marsh, S., and A. Holland (2016). Comprehensive fault database and interpretive fault map of Oklahoma, Oklahoma Geol. Surv. Open-File Rept. OF2-2016, Oklahoma Geological Survey, Norman, Oklahoma.
- Mayeda, K., L. Malagnini, and W. R. Walter (2007). A new spectral ratio method using narrow band coda envelopes: Evidence for non-self-similarity in the Hector Mine sequence, Geophys. Res. Lett. 34, L11303, doi: 10.1029/2007GL030041.
- McGuire, J. J., M. S. Boettcher, and T. H. Jordan (2005). Foreshock sequences and short-term earthquake predictability on East Pacific Rise transform faults, Nature 434, 457-461.
- McLaskey, G. C. (2019). Earthquake initiation from laboratory observations and implications for foreshocks, J. Geophys. Res. 124, no. 12, 12,882-12,904.
- McLaskey, G. C., and B. D. Kilgore (2013). Foreshocks during the nucleation of stick-slip instability, J. Geophys. Res. 118, no. 6, 2982-2997.
- McLaskey, G. C., and D. A. Lockner (2014). Preslip and cascade processes initiating laboratory stick-slip, J. Geophys. Res. 119,
- McLaskey, G. C., and D. A. Lockner (2018). Shear failure of a granite pin traversing a sawcut fault, Int. J. Rock Mech. Min. Sci. 110, 97-110.
- Mueller, C. S. (1985). Source pulse enhancement by deconvolution of an empirical Green's function, Geophys. Res. Lett. 12, no. 1, 33-36.
- Nielsen, S., J. Taddeucci, and S. Vinciguerra (2010). Experimental observation of stick-slip instability fronts, Geophys. J. Int. 180, no. 2, 697-702.
- Noda, H., M. Nakatani, and T. Hori (2013). Large nucleation before large earthquakes is sometimes skipped due to cascade-up-Implications from a rate and state simulation of faults with hierarchical asperities, J. Geophys. Res. 118, 2924-2952.
- Ohnaka, M., and Y. Kuwahara (1990). Characteristic features of local breakdown near a crack-tip in the transition zone from nucleation to unstable rupture during stick-slip shear failure. Tectonophysics 175, nos. 1/3, 197-220.
- Okubo, P. G., and J. H. Dieterich (1984). Effects of physical fault properties on frictional instabilities produced on simulated faults, J. Geophys. Res. 89, no. B7, 5817-5827.
- Rice, J. R. (1993). Spatio-temporal complexity of slip on a fault, J. Geophys. Res. 98, no. B6, 9885-9907.
- Rubin, A. M., and J. P. Ampuero (2005). Earthquake nucleation on (aging) rate and state faults, J. Geophys. Res. 110, no. B11, doi: 10.1029/2005JB003686.
- Ruiz, S., M. Metois, A. Fuenzalida, J. Ruiz, F. Leyton, R. Grandin, C. Vigny, R. Madariaga, and J. Campos(2014). Intense foreshocks and a slow slip event preceded the 2014 Iquique Mw 8.1 earthquake, Science 345, no. 6201, 1165-1169.

- Schaal, N., and N. Lapusta (2019). Microseismicity on patches of higher compression during larger-scale earthquake nucleation in a rate-and-state fault model, J. Geophys. Res 124, 1962-1990.
- Schoenball, M., and W. L. Ellsworth (2017). A systematic assessment of the spatiotemporal evolution of fault activation through induced seismicity in Oklahoma and southern Kansas, J. Geophys. Res. 122, no. 12, 10-189.
- Schoenball, M., F. R. Walsh, M. Weingarten, and W. L. Ellsworth (2018). How faults wake up: The Guthrie-Langston, Oklahoma earthquakes, The Leading Edge 37, no. 2, 100-106.
- Scholz, C. H. (1988). The critical slip distance for seismic faulting, Nature 336, 761-763.
- Scholz, C. H. (1998). Earthquakes and friction laws, Nature 391, no. 6662, 37-42.
- Schurr, B., G. Asch, S. Hainzl, J. Bedford, A. Hoechner, M. Palo, R. Wang, M. Moreno, M. Bartsch, Y. Zhang, O. Oncken, et al. (2014). Gradual unlocking of plate boundary controlled initiation of the 2014 Iquique earthquake, Nature 512, no. 7514, 299-302.
- Shelly, D. R., G. C. Beroza, and S. Ide (2007). Non-volcanic tremor and low-frequency earthquake swarms, Nature 446, no. 7133, 305-307.
- Tinti, E., P. Spudich, and M. Cocco (2005). Earthquake fracture energy inferred from kinematic rupture models on extended faults, J. Geophys. Res. 110, no. B12, doi: 10.1029/2005JB003644.
- Tse, S. T., and J. R. Rice (1986). Crustal earthquake instability in relation to the depth variation of frictional properties, J. Geophys. Res. 91, 9452-9472.
- USGS (2016). Magnitude 5.8 earthquake in Oklahoma, available at https://www.usgs.gov/news/magnitude-56-earthquake-oklahoma (last accessed March 2022).
- Veedu, D. M., and S. Barbot (2016). The Parkfield tremors reveal slow and fast ruptures on the same asperity, Nature 532, 361-365.
- Waldhauser, F. (2001). hypoDD-A program to compute double-difference hypocenter locations, U.S. Geol. Surv. Open-File Rept. 2001-113, doi: 10.3133/ofr01113.
- Waldhauser, F., and W. L. Ellsworth (2000). A double-difference earthquake location algorithm: Method and application to the northern Hayward fault, California, Bull. Seismol. Soc. Am. 90, no. 6, 1353-1368.
- Wu, B. S., and G. C. McLaskey (2019). Contained laboratory earthquakes ranging from slow to fast, J. Geophys. Res. 124, no. 10, 10,270-10,291.
- Wu, Q., M. Chapman, and X. Chen (2018). Stress-drop variations of induced earthquakes in Oklahoma. Bull. Seismol. Soc. Am. 108, no. 3A, 1107-1123.
- Yeck, W. L., G. P. Hayes, D. E. McNamara, J. L. Rubinstein, W. D. Barnhart, P. S. Earle, and H. M. Benz (2017). Oklahoma experiences largest earthquake during ongoing regional wastewater injection hazard mitigation efforts, Geophys. Res. Lett. 44, no. 2, 711-717.
- Yoon, C. E., N. Yoshimitsu, W. L. Ellsworth, and G. C. Beroza (2019). Foreshocks and mainshock nucleation of the 1999 Mw 7.1 Hector Mine, California, earthquake, J. Geophys. Res. 124, no. 2, 1569–1582.
- Ziv, A., and A. M. Rubin (2000). Static stress transfer and earthquake triggering: No lower threshold in sight? J. Geophys. Res. 105, no. B6, 13,631-13,642.

Manuscript received 7 July 2021 Published online 14 April 2022